Comparison of Segmentation Methods for Melanoma Diagnosis in Dermoscopy Images

Margarida Silveira, *Member, IEEE*, Jacinto C. Nascimento, *Member, IEEE*, Jorge S. Marques, André R. S. Marçal, *Member, IEEE*, Teresa Mendonça, *Member, IEEE*, Syogo Yamauchi, Junji Maeda, *Member, IEEE*, and Jorge Rozeira

***Abstract*—In this paper, we propose and evaluate six methods for the segmentation of skin lesions in dermoscopic images. This set includes some state of the art techniques which have been successfully used in many medical imaging problems (gradient vector flow (GVF) and the level set method of Chan *et al.* [(C-LS)]. It also includes a set of methods developed by the authors which were tailored to this particular application (adaptive thresholding (AT), adaptive snake (AS), EM level set [(EM-LS), and fuzzy-based split-and-merge algorithm (FBSM)]. The segmentation methods were applied to 100 dermoscopic images and evaluated with four different metrics, using the segmentation result obtained by an experienced dermatologist as the ground truth. The best results were obtained by the AS and EM-LS methods, which are semi-supervised methods. The best fully automatic method was FBSM, with results only slightly worse than AS and EM-LS.**

***Index Terms*—Dermoscopy, melanoma, segmentation, skin lesion.**

I. Introduction

MALIGNANT melanoma is the most frequent type of skin cancer and its incidence has been rapidly increasing over the last few decades [2]. Nevertheless, it is also the most treatable kind of skin cancer, if diagnosed at an early stage. The clinical diagnosis of melanoma is commonly based on the ABCD rule [21], an analysis of four parameters (asymmetry, border irregularity, color, and dimension), or the 7-points checklist [1] which is a scoring method for a set of different characteristics depending on color, shape, and texture.

Dermoscopy is a non-invasive diagnosis technique for the *in vivo* observation of pigmented skin lesions used in dermatology [2]. Dermoscopic images have great potential in the early diagnosis of malignant melanoma, but their interpretation is time consuming and subjective, even for trained dermatologists [3]. Therefore, there is currently a great interest in the development of computer-aided diagnosis systems that can assist the clinical evaluation of dermatologists. The standard approach in automatic dermoscopic image analysis has usually three stages: 1) image segmentation; 2) feature extraction and feature selection; and 3) lesion classification. The segmentation stage is one of the most important since it affects the accuracy of the subsequent steps. However, segmentation is difficult because of the great variety of lesion shapes, sizes, and colors along with different skin types and textures. In addition, some lesions have irregular boundaries and in some cases there is a smooth transition between the lesion and the skin. Other difficulties are related to the presence of dark hair covering the lesions and the existence of specular reflections. Some of these difficulties are illustrated in Fig. 1.

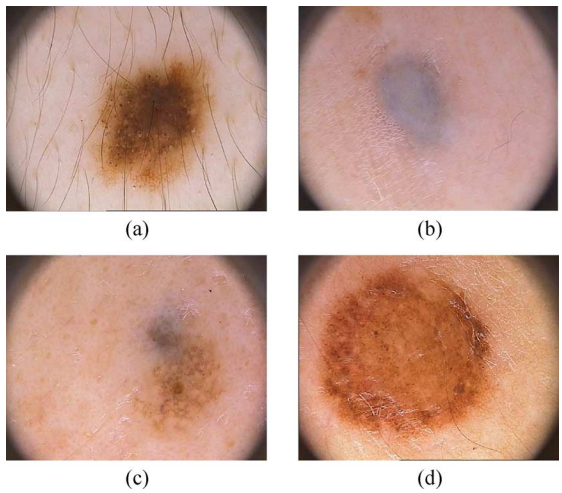

Fig. 1. Difficulties of dermoscopic images; (a) presence of hair; (b) smooth transition between lesion and skin; (c) multiple colored lesions; and (d) specular reflections.

To address this problem, several algorithms have been proposed. They can be broadly classified as thresholding, edge-based or region-based methods. An example of thresholding can be found in [12], where a fusion of global thresholding, adaptive thresholding, and clustering is used. Thresholding methods achieve good results when there is good contrast between the lesion and the skin, thus the corresponding image histogram is bimodal, but usually fail when the modes from the two regions overlap. Edge-based approaches were used in [26] where the

Manuscript received April 15, 2008; revised October 15, 2008. Current version published February 19, 2009. This work was supported by the Fundação para a Ciência e a Tecnologia (ISR/IST plurianual funding) through the POS Conhecimento Program that includes FEDER funds. The associate editor coordinating the review of this manuscript and approving it for publication was Dr. Rangaraj M. Rangayyan.

M. Silveira, J. C. Nascimento, and J. S. Marques are with the Institute for Systems and Robotics and Instituto Superior Técnico, Technical University of Lisbon, Lisbon, Portugal (e-mail: msilveira@isr.ist.utl.pt; jan@isr.ist.utl.pt; jsm@isr.ist.utl.pt).

A. R. S. Marçal and T. Mendonça are with the Faculdade de Ciências da Universidade do Porto, Departamento de Matemática Aplicada, Porto, Portugal (e-mail: tmendo@fc.up.pt; andre.marcal@fc.up.pt).

S. Yamauchi and J. Maeda are with the Department of Computer Science and Systems Engineering, Muroran Institute of Technology, Muroran 050-8585, Japan (e-mail: yama@ipcv.csse.muroran-it.ac.jp; junji@csse.muroran-it.ac.jp).

J. Rozeira is with the Departamento de Dermatologia, Hospital Pedro Hispano, Matosinhos, Portugal.

Color versions of one or more of the figures in this paper are available online at http://ieeexplore.ieee.org.

Digital Object Identifier 10.1109/JSTSP.2008.2011119

segmentation is based on the zero-crossings of the Laplacian-of-Gaussian and in several active contour methods like the gradient vector flow (GVF) used in [11] and the geodesic active contour model (GAC) and the geodesic edge tracing described in [10]. Edge-based approaches perform poorly when the boundaries are not well defined, for instance when the transition between skin and lesion is smooth. In these situations, the edges have gaps and the contour may leak through them. Another difficulty is the presence of spurious edge points that do not belong to the lesion boundary. They are the result of artifacts such as hair, specular reflections or even irregularities in the skin texture and they may stop the contour preventing it to converge to the lesion boundary. Region-based approaches have also been used. Some examples include the multiscale region growing described in [6], the modified fuzzy c-means algorithm which is orientation sensitive proposed in [28], the morphological flooding used in [27], a multiresolution Markov random field algorithm [13] and statistical region merging [7]. Region-based approaches have difficulties when the lesion or the skin region are textured or have different colors present, which leads to oversegmentation.

While several individual techniques have been proposed for the segmentation of lesions in dermoscopic images, only one previous study [31] compared the performance of different techniques. In that study, six different techniques were evaluated; adaptive thresholding [5], fuzzy c-means [16], spherical coordinate transform (SCT)/center split [30], principal components transform (PCT)/median cut [30], split and merge [25], and multiresolution segmentation [25]. No edge-based techniques were tested and only one metric was used to evaluate the methods.

In this paper we propose and evaluate several segmentation methods of the three classes: thresholding, edge-based, and region-based. These algorithms are applied to 100 dermoscopic images of melanocytic lesions and are compared with the expected lesion segmentation (ground truth) obtained by an experienced dermatologist. The evaluation is based on four different metrics that take into account different types of error with distinct clinical relevance. We also make a separate evaluation of the methods when applied to different types of lesions (melanomas, dysplasic nevi, or melanocytic nevi). Preliminary results of this work were published in [20] and [29].

II. Segmentation Methods

We propose and compare six different segmentation methods of the three types: thresholding, edge-based, and region-based. The methods are:

- adaptive thresholding (AT);
- gradient vector flow (GVF);
- adaptive snake (AS);
- level set method of Chan *et al.* (C-LS);
- expectation-maximization level set (EM-LS);
- fuzzy-based split-and-merge algorithm (FBSM).

Their main characteristics, namely method type, region model, and features used, are summarized in Table I. Although fully unsupervised segmentation would be desirable, some of these methods require some degree of user interaction in order to achieve good performance. Therefore, we also include in Table I, the number of mouse clicks required by each of the segmentation methods. The following sections describe each of the methods in more detail.

TABLE I
Summary of the Segmentation Methods Tested

Method	Type	Region Model	Feature	User interaction
AT	Threshold	None	Histogram	None
GVF	Edge	B-spline	Gradient	None
AS	Edge	B-spline	Strokes	2 Mouse clicks
C-LS	Region	None	Color	2 Mouse clicks
EM-LS	Region	None	Color	2 Mouse clicks
FBSM	Region	None	Color and texture	None

A. Adaptive Thresholding (AT)

Lesion segmentation can be obtained by comparing the color of each pixel with a threshold T. The pixel is classified as active (lesion) if it is darker than the threshold. The output of this step is a binary image. Morphological post-processing is then applied to fill the holes and to select the largest connected component in the binary image.

It was experimentally found that the blue component in the red-green-blue (RGB) representation is the one which allows the best discrimination in most dermoscopic images. However, there are a few exceptions. We have therefore used an automatic selection of the color component based on the entropy of the color component i

$$S(i) = -\sum_{k=0}^{L-1} h_i(k) \log[h_i(k)] \tag{1}$$

where $h_i(k)$ is the histogram of the color component i. We assume that the image $I_i(x, y)$ varies in the range $\{0, \ldots, 255\}$ and the histogram is computed using $L = 25$ bins of length 10, after the dark corners were discarded (see Section III-A). We select the color plane with highest entropy:

$$i^* = \arg\max_c S(i). \tag{2}$$

The threshold is automatically computed from the histogram of the selected color component $h_{i^*}(k)$. If the histogram has two major components the threshold can be easily chosen from the local minima between the maxima plus a small offset to account for quantization issues

$$T = T_{valley} + T_1. \tag{3}$$

If the histogram has a single component then the threshold is obtained from the smallest intensity value plus an offset

$$T = T_{\min} + T_2 \tag{4}$$

$T_{\min}$ is obtained in a robust way as the 5-percentile of the image values at the selected color plane $I_{i^*}(x, y)$ in a rectangular region located at the center of the image. The size of this region is 30% of the image size. The offsets T_1 and T_2 were established empirically.

B. Gradient Vector Flow (GVF)

The GVF snake is a well-known algorithm proposed in [32] which has been successfully used in many medical imaging

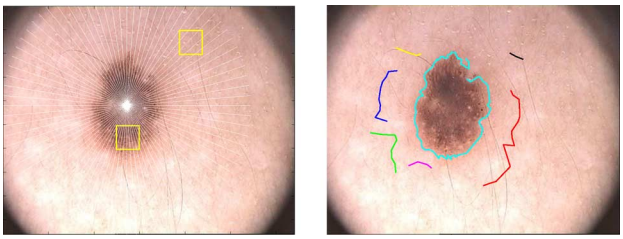

Fig. 2. Radial lines and windows selected by the user (left) and detected segments (right).

problems. The object boundary is approximated by an elastic contour $\mathbf{x}(s) = (x(s), y(s)), s \in [0,1]$ which is initialized in the image domain by the user or by heuristic criteria. The elastic contour is then modified according to the differential equation

$$\frac{\partial \mathbf{x}_{(s,t)}}{\partial t} = \mathbf{F}_{int}(\mathbf{x}(s,t)) + \mathbf{v}(\mathbf{x}(s,t)) \tag{5}$$

where $\mathbf{F}_{int}$ is an internal force, similar to the one used in traditional snakes [15] that tries to keep the shape's continuity and smoothness, and $\mathbf{v} = (u(x,y), v(x,y))$ is the GVF field. The GVF field $\mathbf{v}$ is a regularized version of the image or edge gradient which allows long range attraction of the contour towards the object boundary, even if the contour is located in homogeneous regions where the gradient is zero. $\mathbf{v}$ is obtained by minimizing the energy

$$E = \int\int \mu(u_x^2 + u_y^2 + v_x^2 + v_y^2) + |\nabla f|^2 |\mathbf{v} - \nabla f|^2) \tag{6}$$

where f is the image edge map.

The initialization of the GVF snake is automatic. A circle with a given radius is placed on the image. The circle center is given by the center of the segmented region obtained by the Adaptive Threshold method. The circle radius is such that the model units are far away from the features of interest.

More details concerning this method can be found in [32]. We have used the source code provided in http://iacl.ece.jhu.edu/projects/gvf/ .

C. Adaptive Snake (AS)

Active contours are often attracted by spurious edges which do not belong to the lesion boundary. These normally appear in dermoscopic images due to artifacts such as hair, specular reflections or even from variations in the skin texture. Therefore, we need robust methods which are able to discard the influence of outlier edges. The adaptive snake tries to achieve this goal [22].

First, the method detects contour segments (strokes) in the image, using edge linking, and then approximates a subset of them using a robust estimation algorithm based on the expectation-maximization (EM) [19] algorithm.

Stroke detection is done in two steps. First, we detect intensity transitions along a set of radial directions (see Fig. 2, left) using correlation matching in the hue saturation value (HSV) color space [4]. Edge linking is then performed adopting simple continuity criteria (see Fig. 2 right). User intervention is required to select the regions used to compute the color statistics (two mouse clicks).

Let us briefly describe the robust estimation of the contour. Only a subset of the detected strokes are valid and should be considered. We therefore assign a confidence degree associated with each stroke using the EM method.

TABLE II
ADAPTIVE SNAKE

Adaptive Snake
Strokes detection: Detect edge points in the image by radial analysis and organize them in strokes, using an edge-linking operation
EM method: initialize contour $\mathbf{x}$ and iterate
E-step: For each stroke $\mathbf{y}^j$ compute the confidence degree $w^j \propto p(\mathbf{y}^j \mid k^j = 1, \hat{\mathbf{x}}) P(k^j).$
M-step: Update the contour model by $\hat{\mathbf{x}}^{(t+1)} = \hat{\mathbf{x}}^{(t)} - \gamma \nabla_x Q(\mathbf{x}; \hat{\mathbf{x}}^{(t)})$

Let $\mathbf{y}$ be the set of all the features detected in the image; $\mathbf{y} = \{\mathbf{y}^1, \ldots, \mathbf{y}^N\}$, where $\mathbf{y}^j$ is the j-th stroke and $\mathbf{k} = \{k^1, \ldots, k^N\}$ is the set of binary labels (valid—invalid) associated to the strokes. Let $\mathbf{x}$ be a contour model defined by a sequence of 2-D points $\mathbf{x}_i$ $i = 1, \ldots, M$. The goal is to approximate the data contained in $\mathbf{y}$, or a subset of it, by the contour model $\mathbf{x}$, using the *maximum a posteriori* (MAP) criterion

$$\hat{\mathbf{x}} = \arg\max_x \log p(\mathbf{y}, \mathbf{k}, \mathbf{x}). \tag{7}$$

Since $\mathbf{k}$ is not known, we cannot estimate $\mathbf{x}$ using (7). The EM algorithm overcomes this difficulty by replacing $\log p(\mathbf{y}, \mathbf{k}, \mathbf{x})$ by its expected value with respect to the hidden variable $\mathbf{k}$, i.e.,

$$Q(\mathbf{x}; \hat{\mathbf{x}}) = E_{\mathbf{k}}\Big\{\log p(\mathbf{y}, \mathbf{k}, \mathbf{x}) \mid \mathbf{y}, \hat{\mathbf{x}}\Big\} \tag{8}$$

where $\hat{\mathbf{x}}$ is the best available estimate of $\mathbf{x}$. After straightforward manipulation

$$Q(\mathbf{x}; \hat{\mathbf{x}}) = \mathrm{C} + \sum_i \mathcal{P}_a(\mathbf{x}_i, \mathbf{y}) + E_{int}(\mathbf{x}) \tag{9}$$

where C is a constant; E_{int} is the internal energy as before; $\mathcal{P}_a(\mathbf{x}_i, \mathbf{y})$ is a new potential function given by

$$\mathcal{P}_a(\mathbf{x}_i, \mathbf{y}) = -\sum_j w^j P^j(\mathbf{x}_i) \tag{10}$$

where $P^j(\mathbf{x}_i)$ is the potential function associated to the j-th stroke and w^j is the corresponding confidence degree i.e., the probability that the j-th stroke is valid

$$w^j = P(k^j = 1 | \mathbf{y}^j, \hat{\mathbf{x}}) \tag{11}$$

(see details in [22]). The potential function $\mathcal{P}_a$ varies during the estimation process. It is therefore called *adaptive potential*.

The EM method recursively updates the elastic contour in two steps. The E-step updates the stroke confidence degrees w^j based on the most recent estimate of the contour. Then, the M-step maximizes the $Q(\mathbf{x}, \hat{\mathbf{x}})$ using the gradient algorithm. These steps are summarized in Table II. A detailed description can be found in [22].

Fig. 3 shows the evolution of the adaptive potential during the convergence process, for the segmentation of the image in

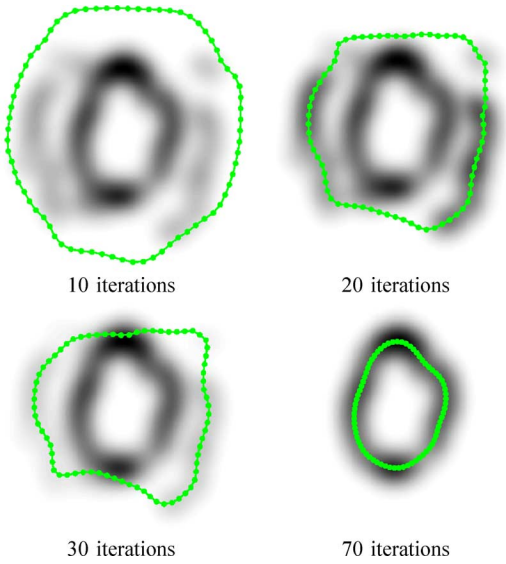

Fig. 3. Evolution of the adaptive potential during the convergence process.

Fig. 2. The valleys associated to outlier strokes disappear as they receive negligible weights.

The AS used the same initialization as the GVF snake technique.

D. Level Set Method of Chan et al. (C-LS)

The first region-based method used in this study is the level set algorithm proposed in [8] for vector valued images. It assumes that the image I is formed by two regions of approximately piecewise constant intensity c_1 and c_2 separated by a curve C. Considering an image with N channels, each denoted by I_i, the following energy function is defined:

$$F(c_1,c_2,C) = \mu\, length(C) + \lambda_1 \int_{inside(C)} \frac{1}{N}\sum_{i=1}^{N} |I_i(x)-c_{1,i}|^2 dx + \lambda_2 \int_{outside(C)} \frac{1}{N}\sum_{i=1}^{N} |I_i(x)-c_{2,i}|^2 dx. \quad (12)$$

In this equation, the first term is a regularizing term that depends on the length of the curve, μ; λ_1, λ_2 are positive weighting parameters and the last two terms are the fitting terms of I averaged over all the channels. In the present case, the original RGB images were processed in the $L^\star$, $a^\star$ and $b^\star$ color space and therefore three channels are used.

Using the level set formulation [23], embedding the curve C as the zero level set $C(t) = \{(x)|\phi(t,x) = 0\}$ of a higher dimensional level set function $\Phi(t,x)$ this energy function can be rewritten as

$$E(\Phi,c_1,c_2) = \mu \int_\Omega \delta(\Phi)\,|\nabla\Phi|\,dx + \int_\Omega \begin{bmatrix} \frac{1}{N}\sum_{i=1}^{N} \lambda_1 |I_i(x)-c_{1,i}|^2 H(\Phi) \\ +\frac{1}{N}\sum_{i=1}^{N} \lambda_2 |I_i(x)-c_{2,i}|^2 (1-H(\Phi)) \end{bmatrix} dx \quad (13)$$

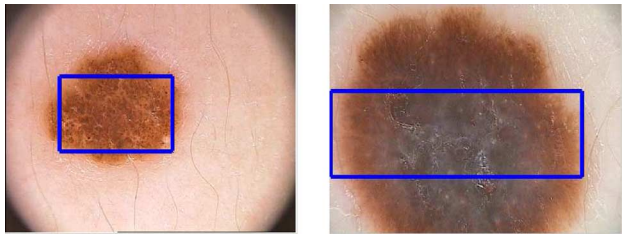

Fig. 4. Initial contours used by the C-LS and EM-LS method for two of the images in our data set.

where H is the Heaviside function, $H(z) = 1$ for $z \geq 0$ and $H(z) = 0$ for $z < 0$. The evolution of Φ is governed by the following motion partial differential equation (PDE):

$$\frac{\partial\Phi}{\partial t} = \delta_\varepsilon(\Phi) \begin{bmatrix} \mu div\left(\frac{\nabla\Phi}{|\nabla\Phi|}\right) \\ -\frac{1}{N}\sum_{i=1}^{N} \lambda_1 |I_i(x)-c_{1,i}|^2 \\ +\frac{1}{N}\sum_{i=1}^{N} \lambda_2 |I_i(x)-c_{2,i}|^2 \end{bmatrix} \quad (14)$$

where $\delta_\varepsilon(\Phi)$ is a regularized version of the Dirac delta function. Each $c_{1,i}$ and $c_{2,i}$ is updated by the average of the i-th channel I_i calculated $inside(C)$ and $outside(C)$, respectively. The evolution is solved using finite differences.

In this experiment the initialization was done using a rectangle placed by the user in the lesion region (2 mouse clicks). The initialization does not need to be very close to the final boundary, it can be inside, outside or across the lesion, but it is important that the significant lesion colors are represented in the initial contour. Fig. 4 shows some of the initializations used in the experiments.

E. Expectation-Maximization Level Set Method (EM-LS)

The method described in this section is an extension of the Level Set method of Chan *et al.* presented in the previous section. The assumption that the two regions have piecewise constant densities is too restrictive; it is not a good model to represent the different colors that are usually present in both the lesions and the skin. Therefore, this method proposes a more flexible approach which assumes that the intensities of regions inside and outside C are modeled by probability density functions p_1 and p_2, respectively. The adopted model for p_1 and p_2 density functions is the mixture of Gaussians, and at every iteration of the level set algorithm the parameters of the mixture model are estimated with the expectation-maximization (EM) algorithm [19].

The segmentation is obtained by minimizing the energy function

$$E(p_1,p_2,C) = \mu\, length(C) - \lambda_1 \int_{inside(C)} \log p_1(I|\theta_1)dx - \lambda_2 \int_{outside(C)} \log p_2(I|\theta_2)dx \quad (15)$$

where μ, λ_1, λ_2 are positive weighting parameters and θ_1, θ_2 are the parameters of probability density functions p_1 and p_2, respectively. This equation extends (12).

Using the level set formulation [23], embedding the curve C as the zero level set $C(t) = \{(x)|\phi(t,x) = 0\}$ of a higher dimensional level set function $\Phi(t,x)$ this energy function can be rewritten as

$$E(\Phi, p_1, p_2) = \mu \int_\Omega \delta(\Phi)\,|\nabla\Phi|\,dx - \int_\Omega [\lambda_1 H(\Phi)\log p_1(I|\theta_1) + \lambda_2(1-H(\Phi))\log p_2(I|\theta_2)]\,dx \tag{16}$$

where H is the Heaviside function defined in Section II-D. This equation extends (13).

The evolution of Φ is governed by the following motion PDE:

$$\frac{\partial\Phi}{\partial t} = \delta_\varepsilon(\Phi)\begin{bmatrix}\mu div\left(\frac{\nabla\Phi}{|\nabla\Phi|}\right) - \lambda_1\log p_1(I|\hat{\theta}_1)\\ +\lambda_2\log p_2(I|\hat{\theta}_2)\end{bmatrix} \tag{17}$$

where $\delta_\varepsilon(\Phi)$ is a regularized version of the Dirac delta function. This equation extends (14).

We model both probability density functions as a mixture of Gaussians

$$p(I|\theta) = \sum_{m=1}^{K}\alpha_m p(I|\theta_m) \tag{18}$$

where K is the number of components, $\alpha_1 \ldots \alpha_K$ are the mixing probabilities summing to one, and each θ_m is the set of parameters of the m-th component. Since Gaussian components are assumed, we have $\theta_m = [\mu_m, R_m]$, where μ_m represents the mean and R_m represents the covariance.

At every iteration of the level set method the mixture of Gaussians is estimated with the EM algorithm [19]. The EM algorithm alternates between two steps. In the E-step, a set of weights summing to one is assigned to each region point I^j, $j = 1,\ldots,N$, where I^j has 3 components, corresponding to the $L^\star$, $a^\star$ and $b^\star$ color channels

$$w_k^j = \frac{\alpha_k p(I^j|\hat{\theta}_k)}{\sum_{m=1}^{K}\alpha_m p(I^j|\hat{\theta}_m)} \tag{19}$$

where $\hat{\theta}_m$ denotes the estimate of parameters for the m-th component obtained in the previous iteration.

In the M-step, the parameters of each component are updated

$$\mu_k = \frac{\sum_{j=1}^{N} w_k^j I^j}{\sum_{j=1}^{N} w_k^j} \tag{20}$$

$$R_k = \frac{\sum_{j=1}^{N} w_k^j (I^j-\mu_k)(I^j-\mu_k)^T}{\sum_{j=1}^{N} w_k^j}. \tag{21}$$

The mixing proportions are updated by

$$\alpha_k = \tfrac{1}{N}\sum_{j=1}^{N} w_k^j. \tag{22}$$

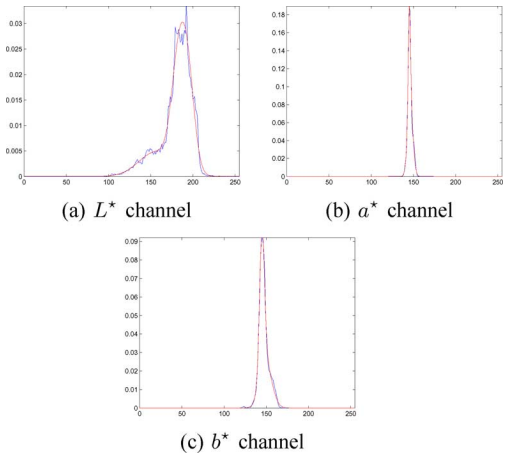

(a) $L^\star$ channel (b) $a^\star$ channel

(c) $b^\star$ channel

Fig. 5. Comparison between histogram in the lesion region and pdf estimated by the EM-LS method for the image in Fig. 1(c).

Fig. 5 compares the histogram of intensity values in the lesion regions with the pdf's estimated with the EM algorithm for the three color channels ($L^\star$, $a^\star$ and $b^\star$) from the image in Fig. 1(c). The histogram is shown in blue and the pdf is shown in red. It can be seen that the two curves are very close thus the adopted model is a good approximation.

If the regions were modeled by single Gaussian densities and we assumed that the covariance matrix is the same for both regions and satisfied $R = \sigma^2 I_n$ where $I_n \in \mathbb{R}^{n\times n}$ is the identity matrix of dimension $n \times n$, we would get the model adopted in the Chan *et al.* method

$$\log p_i = C_0 - C_1\,\|I-\mu_i\|^2\,. \tag{23}$$

This method used the same initialization as the C-LS method described in the previous section.

F. Fuzzy-Based Split-and-Merge Algorithm (FBSM)

The sixth method used in this study is a fuzzy-based split-and-merge algorithm (FBSM), recently proposed in [17], [18]. The algorithm originally aims at unsupervised perceptual segmentation of natural color images. Since the algorithm has the significant advantage to stop the process at the specified number of segmented regions, it is applicable to the segmentation of dermoscopic images. First, the FBSM algorithm extracts color features and texture features from an original image. The values of $L^\star$, $a^\star$ and $b^\star$ are used as color features, and the statistical geometrical features (SGF) [9] are used as texture features. Then, a split-and-merge technique is executed in four stages: simple splitting, local merging, global merging and boundary refinement. During the latter three stages, the similarity of any adjacent regions is estimated using the fuzzy-based homogeneity measure that combines the similarity of color features and texture features with different degrees of importance. The adoption of a fuzzy-based homogeneity measure simplifies the complex mechanism of integrating different features by means of symbolic representations.

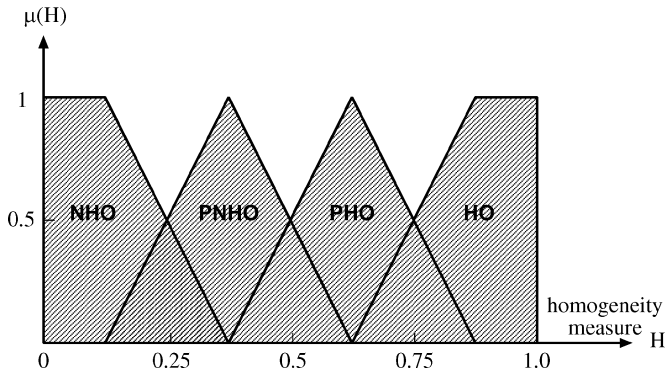

Fig. 6. Fuzzy sets used for homogeneity inference. HO stands for homogeneous, NHO is not homogeneous, PHO is probably homogeneous, and PNHO is probably not homogeneous.

The following fuzzy rules are used in which each rule has a corresponding membership function.

1) Rule 1: *If* SGF difference is SMALL, *Then* HOMOGENEOUS (HO); *Else* NOT_ HOMOGENEOUS (NHO).
2) Rule 2: *If* $L^{\star}a^{\star}b^{\star}$ difference is SMALL, *Then* PROBABLY_ HOMOGENEOUS (PHO); *Else* PROBABLY_ NOT_ HOMOGENEOUS (PNHO).

After fuzzification by applying the above two rules, min-max inference takes place using the fuzzy sets shown in Fig. 6. Then the conventional centroid defuzzification method is applied. Suppose the homogeneity limit is set to be 0.5. Then, if the inferred homogeneity measure is over 0.5, the two regions being concerned are regarded as homogeneous and they are merged.

The split-and-merge procedure starts from simple splitting in which an original image is divided into rectangular subblocks of size 4×4. Local merging is a stage to merge adjacent regions locally for drastically reducing the number of regions to be used at the stage of global merging. Global merging is a stage to merge similar adjacent regions globally. Since global merging reduces the number of segmented regions one by one at each step, and it removes the less important regions first, the essential regions remain to the end and thus perceptual segmentation is achieved. It is also easy to stop the algorithm at the specified number of segmented regions. The expected number of segmented regions used for dermoscopic images is 2. Boundary refinement is finally performed to smooth the jagged boundaries after global merging.

The implementation of the FBSM algorithm is fully automatic, because the parameters required by the algorithm are automatically tuned based on the information extracted from the image.

III. Image and Ground Truth Acquisition

The clinical database of Hospital Pedro Hispano (HPH) has over 4000 cases with dermoscopic images of various types of lesions, all of them obtained under the same conditions through Tuebinger Mole Analyzer system. A total of 100 dermoscopic images were selected randomly from the database along with the clinical diagnosis, being 35 melanocytic nevi (regular), 25 dysplasic nevi, and 30 melanomas. The images are in 24-bit RGB color, with 768×560 pixels.

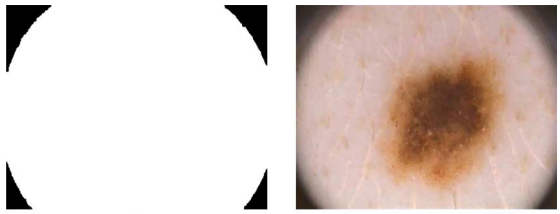

Fig. 7. Preprocessing of the image in Fig. 1(a); (a) mask obtained for corner removal and (b) hair removal.

For each image a manual segmentation was performed in full sized printed images by Dr. Jorge Rozeira (an expert dermatologist with over 8 years of experience in dermoscopic image analysis). The set of manual segmentations were scanned and rectified. The contour of the lesions was identified on these digital images to produce a binary image for each lesion. Therefore the resulting reference binary database is a reliable ground truth in order to access the accuracy of each segmentation produced by the different methods under evaluation.

A. Preprocessing

The images were filtered with the morphological closing filter using a disk as structuring element ($\mathrm{radius} = 5\ \mathrm{pixels}$) in order to remove the features from dark hair and additionally with a median filter (3×3 neighborhood). Then, the dark regions in the four corners of the images were removed. To remove the corners, gray-level thresholding was first performed using Otsu's method [24] followed by elimination of the binary components that were connected to each of the four corners. Fig. 7 illustrates the preprocessing steps.

IV. Evaluation of Segmentation Results

Four different metrics were used to quantify the boundary differences. The Hammoude distance (HM) [14], the true detection rate (TDR) and the false positive rate (FPR) are area based metrics. In addition, we used the Hausdorff distance (HD) which measures the distance between the boundaries in pixels.

To define these metrics let SR denote the result of an automatic segmentation method and GT denote the ground truth segmentation obtained by the medical expert. Both SR and GT are binary images such that all the pixels inside the curve have label 1 and all the others have label 0. The metrics are calculated as follows:

- Hammoude distance (HM)
  This metric makes a pixel by pixel comparison of the pixels enclosed by the two boundaries:

$$HM(SR, GT) = \frac{\#(SR \cup GT) - \#(SR \cap GT)}{\#(SR \cup GT)} \tag{24}$$

  it takes into account two different types of error; pixels classified as lesion by the medical expert that were not classified as such by the automatic segmentation and pixels classified as lesion by the automatic segmentation

that were not classified as such by the medical expert. The Hammoude distance gives the same importance to both types of error. However, from a clinical point of view, the first type of error is more important since the lesion pixels should never be missed. Therefore, we felt the need to use two separate metrics to take into account the two types of error.

- True detection rate (TDR)
  This metric measures the rate of pixels classified as lesion by both the automatic and the medical expert segmentation:

$$TDR(SR, GT) = \frac{\#(SR \cap GT)}{\#(GT)}. \tag{25}$$

  This metric is also an indirect measure of the False Negative Rate (FNR), since $FNR = 1 - TDR$. The FNR measures the rate of pixels classified as lesion by the medical expert that were not classified as lesion by the automatic segmentation. Clinically, this is worse of the two types of error.
- False positive rate (FPR)
  This metric measures the rate of pixels classified as lesion by the automatic segmentation that were not classified as lesion by the medical expert:

$$FPR(SR, GT) = \frac{\#\left(SR \cap \overline{GT}\right)}{\#(GT)}. \tag{26}$$

- Hausdorff distance (HD)
  The Hausdorff distance finds the largest distance between the boundary points.
  Let $GT = \{gt_1, gt_2, \ldots gt_m\}$ and $SR = \{sr_1, sr_2, \ldots sr_n\}$ denote the set of points belonging to contour GT and contour SR, respectively. The distance from gt_i to its closest point (DCP) in SR is given by

$$d(gt_i, SR) = \min_j \|sr_j - gt_i\|. \tag{27}$$

  The Hausdorff distance is the maximum of the distance to the closest points between the two curves

$$HD(GT, SR) = \max\{\max_i d(gt_i, SR), \max_j d(sr_j, GT)\}. \tag{28}$$

  This metric, like the Hammoude distance, does not distinguish between distance from inside or from outside of the reference curve.

V. Experimental Results

Six different segmentation methods were evaluated, as detailed in Section II. The evaluation was based on the measures described in Section IV, using as ground truth the contours obtained manually by an experienced dermatologist.

The parameters used by each method were the same in all the experiments. The AT method used $T_1 = 10$ and $T_2 = 50$. The GVF and the AS snakes were both initialized with a circle. The center was given by the center of the segmented region obtained by the AT method and the radius was fixed to 400 pixels.

TABLE III
Results of the Segmentation Methods Calculated for the 100 Images. The Values in Bold Correspond to the Best Performance

Method	HM (%)	TDR (%)	FPR (%)	HD (pixels)	Gross Errors (%)
AT	16.20	91.30	4.08	54.67	19
GVF	19.98	90.89	8.67	48.80	16
AS	**12.63**	**95.47**	6.36	**36.90**	**8**
C-LS	19.09	83.39	**2.55**	57.01	22
EM-LS	15.06	95.20	6.17	49.67	11
FBSM	14.73	93.67	3.73	47.04	18

For the GVF snake, the elasticity, rigidity, viscosity, and regularization parameters were $\alpha = 2$, $\beta = .1$, $\gamma = 1$ and $\mathrm{k} = 2$, respectively. The edge map f was computed with the Canny edge operator and the GVF field was computed with $\mu = 0.1$. The AS technique used $\sigma = 15$ and the regions used for correlation matching in the stroke detection step were 50×50 pixels. Both region based level set methods (C-LS and EM-LS) used the same parameters: $\lambda_1 = 10$, $\lambda_2 = 10$, $\mu = 0.5 \times 255^2$. Three components ($K = 3$) were used in the EM-LS method to represent the pdf both in the lesions regions and also for the skin. Using three components, the correlation coefficient between the intensity histogram and the estimated pdf was above 90% for lesion regions and above 86% in the skin regions, for all the images. Using the C-LS method, we obtained significantly smaller correlation coefficients between the intensity histogram and the estimated pdf, as expected (above 33% for lesion region and above 42% in the skin regions). The iterative algorithms stop when either a maximum number of iterations (70) are achieved or when there are no changes in the contour.

All the methods were implemented in Matlab, except for FBSM. The execution time was approximately 2 s per image for the AT, 6 s for the AS, 19 s for the GVF, 150 s for the C-LS, and 190 s for the EM-LS. For the FBSM technique, the time is about 330 s per image.

The experimental results are divided in two parts. First, we evaluate the algorithms using the whole data set of images. Then we discuss the performance of the segmentation methods for three types of lesions which are often found in practice: melanomas, dysplasic nevi, and melanocytic nevi. As we will see, the performance of the segmentation methods is different in these three cases.

A. Evaluation on the Complete Data Set

The database of 100 images was processed using all the methods under evaluation. The segmentation results were compared with the reference images (ground truth) and the segmentation errors were evaluated by the four metrics described above. Table III shows the median of the segmentation scores for each method. The best method according to the Hammoude distance is the AS with a score of 12.63%. The best true detection rate is achieved by the AS and EM level set techniques (95.47% and 95.20%, respectively). The best false positive rate is obtained by the C-LS (2.55%). The Hausdorff distance behaves similarly to the Hammoude distance. The true detection rate is specially important since it measures the fraction of lesion pixels which are detected in all the images.

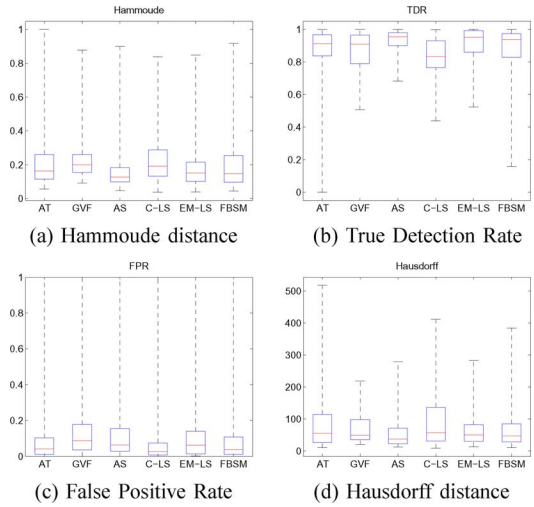

(a) Hammoude distance (b) True Detection Rate

(c) False Positive Rate (d) Hausdorff distance

Fig. 8. Box-plots for the comparison of the segmentation methods. The boxes have lines at the median value and at the 25% and 75% quartile values.

Table III also shows the percentage of gross segmentation errors defined as the rate of segmented images with Hammoude distance greater than 30%, which according to the authors experience corresponds to unacceptable segmentation results. The Adaptive Snake and the EM level set are much more robust than the other methods according to this criterion since the number of gross segmentation errors is much smaller.

Table III does not contain information about the uncertainty associated with these segmentation scores. This information can be evaluated visually in Fig. 8 which displays the median, the 25 and 75 percentiles for all the methods and metrics. All the methods have comparable performance between the 25 and 75 percentile. The main difference concerns the number and amplitude of the outliers (gross segmentation errors).

The Hammoude and Hausdorff distances incorporate two types of error, false positive and false negative, giving equal importance to both of them. However, from a clinical point of view, the false negatives are more important because it is important not to miss any part of the lesion. Therefore, we will focus on the TDR and the FPR. The AS and the EM-LS achieves the best scores in terms of TDR while the C-LS is the best according to the FPR.

We tested if the methods were statistically different using paired Wilcoxon tests for all pairs of methods and for the 4 metrics. The results, at 0.05 significance level, showed that all the methods are statistically different at least with regard to one of the metrics. However, taking only TDR and FPR into account, AS and EM-LS are not statistically different.

It is unfair to compare all these methods without saying that some of them require user intervention (2 mouse clicks) while others are fully automatic. The best results in the first set of methods are achieved by the EM level set and Adaptive Snake while the best fully automatic method is the FBSM.

Figs. 9–14 show examples of the segmentation results for several types of lesions: melanomas, dysplasic nevi and melanocytic nevi. Figs. 9–11 show the segmentation of a melanoma, a dysplasic nevus and a melanocytic nevus. In these cases, all the methods produce segmentation results which are close to the ground truth segmentation. This happens when there is a good contrast between the lesion and the skin, thus

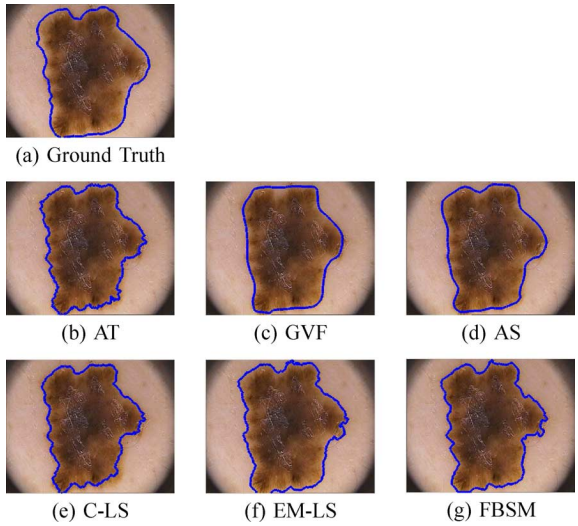

(a) Ground Truth

(b) AT (c) GVF (d) AS

(e) C-LS (f) EM-LS (g) FBSM

Fig. 9. Segmentation of a melanoma.

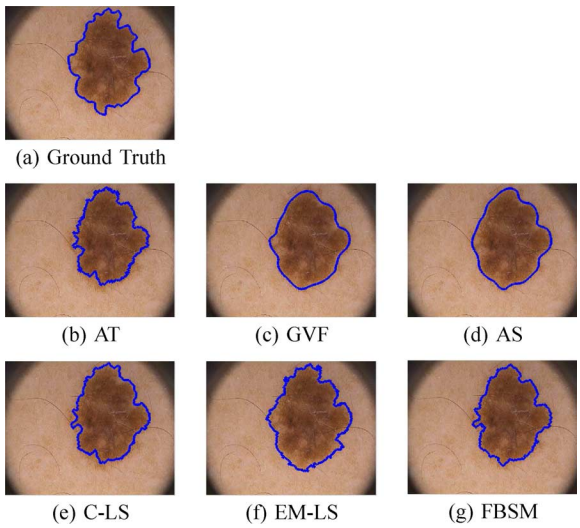

(a) Ground Truth

(b) AT (c) GVF (d) AS

(e) C-LS (f) EM-LS (g) FBSM

Fig. 10. Segmentation of a dysplasic nevus.

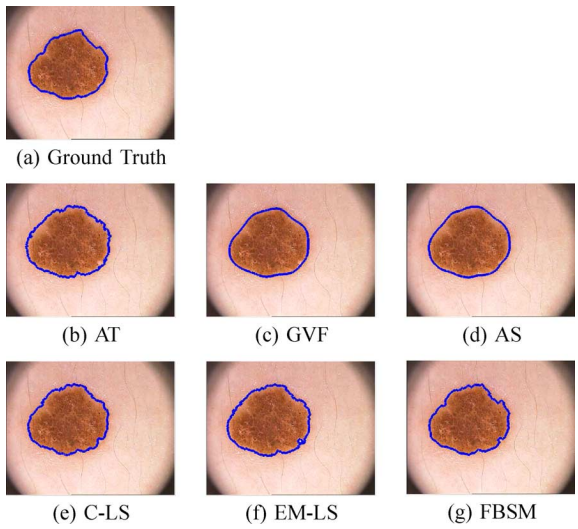

(a) Ground Truth

(b) AT (c) GVF (d) AS

(e) C-LS (f) EM-LS (g) FBSM

Fig. 11. Segmentation of a melanocytic nevus.

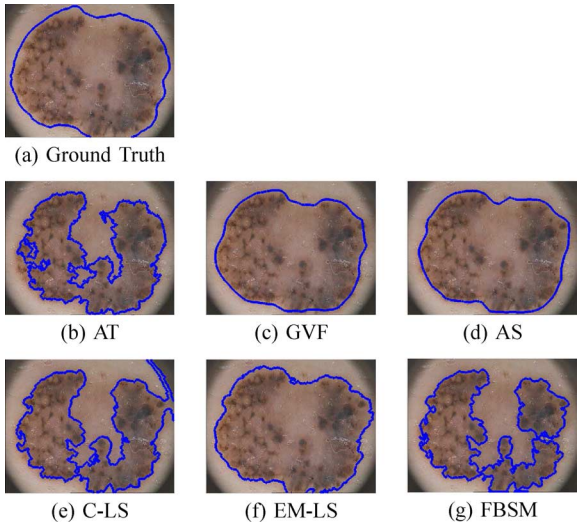

(a) Ground Truth (b) AT (c) GVF (d) AS (e) C-LS (f) EM-LS (g) FBSM

Fig. 12. Segmentation of a melanoma.

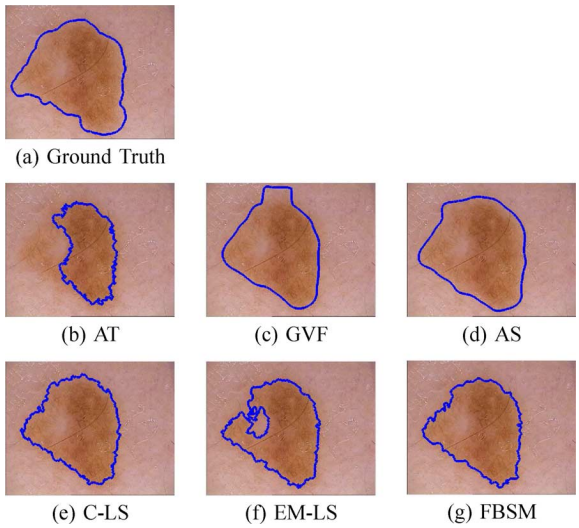

(a) Ground Truth (b) AT (c) GVF (d) AS (e) C-LS (f) EM-LS (g) FBSM

Fig. 13. Segmentation of a melanocytic nevus.

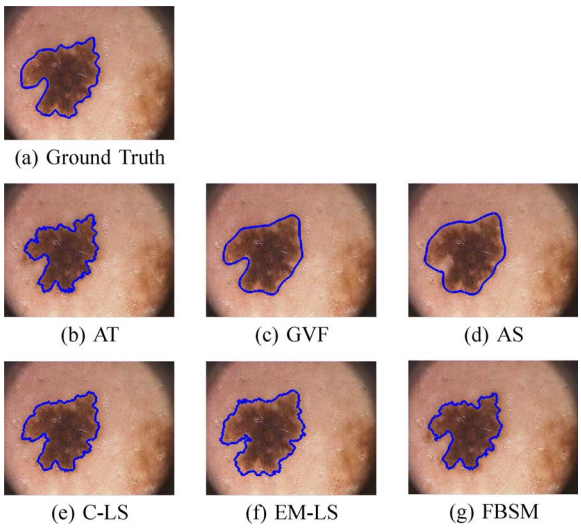

(a) Ground Truth (b) AT (c) GVF (d) AS (e) C-LS (f) EM-LS (g) FBSM

Fig. 14. Segmentation of a melanoma.

the lesion boundaries are well defined. More difficult cases are shown in Figs. 12–14 which correspond to two melanomas and a melanocytic nevus. The melanoma lesion in Fig. 12 contains regions with different visual properties. The center part of the lesion is similar to the normal skin. This image was well segmented only by the methods which require user intervention. The nevus image (Fig. 13) has a very small contrast between the lesion and the skin. Some of the methods (AT, GVF, and EM-LS) fail to produce a good estimate of the boundary. The melanoma lesion in Fig. 14 has pronounced concavities, therefore the region-based methods have better results and the GVF snake converges better than the AS.

These examples suggest that the segmentation algorithms have different performance for different types of images and skin lesions. We will discuss this topic in the Section V-B.

TABLE IV
RESULTS OF THE SEGMENTATION METHODS CALCULATED FOR THE 30 MELANOMA IMAGES. THE VALUES IN BOLD CORRESPOND TO THE BEST PERFORMANCE

Method	HM (%)	TDR (%)	FPR (%)	HD (pixels)	Gross Errors (%)
AT	19.16	86.22	2.17	102.39	27
GVF	25.36	79.48	4.46	111.91	33
AS	**16.24**	**90.63**	4.53	**84.99**	**23**
C-LS	22.00	80.08	**1.63**	134.37	30
EM-LS	18.22	86.99	2.22	99.60	**23**
FBSM	21.29	85.10	1.70	93.84	33

TABLE V
RESULTS OF THE SEGMENTATION METHODS CALCULATED FOR THE 25 DYSPLASIC NEVI. THE VALUES IN BOLD CORRESPOND TO THE BEST PERFORMANCE

Method	HM (%)	TDR (%)	FPR (%)	HD (pixels)	Gross Errors (%)
AT	15.02	90.89	2.57	39.69	8
GVF	20.54	89.39	7.81	46.48	16
AS	**11.88**	95.41	5.55	**37.05**	**4**
C-LS	18.03	86.51	**2.20**	38.21	8
EM-LS	14.65	**95.71**	6.55	41.67	8
FBSM	13.52	94.41	4.78	37.20	**4**

TABLE VI
RESULTS OF THE SEGMENTATION METHODS CALCULATED FOR THE 35 MELANOCYTIC NEVI IMAGES. THE VALUES IN BOLD CORRESPOND TO THE BEST PERFORMANCE

Method	HM (%)	TDR (%)	FPR (%)	HD (pixels)	Gross Errors (%)
AT	15.02	93.12	6.72	36.95	21
GVF	17.81	94.43	13.90	43.01	5
AS	**12.31**	97.41	8.44	**29.31**	**0**
C-LS	18.32	87.28	**3.64**	43.66	21
EM-LS	12.71	**97.56**	9.24	38.50	5
FBSM	12.38	95.33	4.58	37.16	16

B. Separate Evaluation With Different Lesion Types

This section presents a separate evaluation of the segmentation methods when applied to different types of lesions: melanomas, dysplasic nevi and melanocytic nevi. We asked a specialist to visually classify the lesions in the 100 images. For 73% of the melanoma cases and 44% of the dysplasic nevi there was histological confirmation. Two images received not one but two labels (dysplasic nevi and melanoma) and were included in both classes.

Tables IV–VI show the median of the performance measures for each type of lesion.

The main difference concerns the FPR and the TDR. The FPR is smaller in the case of melanomas and dysplasic nevi images but significantly increases in the case of melanocytic nevi due to the lower contrast that characterizes these types of lesions. In addition, the TDR is significantly lower for the melanoma cases than for the melanocytic and dysplasic nevi.

VI. Conclusion

We proposed and evaluated six methods for the segmentation of skin lesions in dermoscopic images. This set includes some state of the art techniques which have been successfully used in many medical imaging problems (Gradient Vector Flow [32] and the Level Set method of Chan *et al.* [8]). It also includes a set of methods developed by the authors which were tailored to this particular application (AT, AS, EM-LS, and FBSM). The methods were applied to a set of 100 dermoscopic images from the clinical database of Hospital Pedro Hispano including 35 melanocytic nevi (regular), 25 dysplasic nevi, and 30 melanomas. These images were segmented manually by an expert dermatologist and the type of lesion was classified. The output of the automatic segmentation methods was compared with the manually segmented images using four different metrics (Hammoude distance, TDR, FPR, and Hausdorff distance). The TDR was considered the most relevant metric from a clinical point of view. The best results were obtained by the AS and EM-LS methods which achieved $\mathrm{TDR} = 95.47\%$ and $\mathrm{TDR} = 95.20\%$, respectively. In addition, these methods were the most robust in this data set since the number of gross errors ($\mathrm{Hammoude\ distance} \leq 30\%$) is 8% and 11%, respectively. However, these two techniques require a small degree of user intervention in their initialization (2 mouse clicks each). Fully automatic methods such as FBSM achieved slightly worse results ($\mathrm{TDR} = 93.67\%$) as expected, with an increase of gross errors to 18%.

We also performed a separate evaluation of the methods for the segmentation of different types of lesion (melanomas, dysplasic nevi, and melanocytic nevi). This kind of analysis has been addressed previously in [11] but considering only melanomas and benign lesions. The methods showed increased TDR for the melanoma cases and also an increased FPR in the case of melanocytic nevi. This is interpreted as due to the low contrast between the lesion and the skin which characterizes this type of lesion.

We believe that the AS and EM-LS methods are robust and useful for the lesion segmentation in a computer aided diagnosis system to assist the clinical diagnosis of dermatologists.

Acknowledgment

The authors wish to thank A. Vieira and A. Rodrigues for the digitalization of the reference segmentations and Dr. M. Pereira and M. Teixeira of hospital Pedro Hispano for help with image selection.

References

[1] G. Argenziano, G. Fabbrocini, P. Carli, V. D. Giorgi, E. Sammarco, and M. Delfino, "Epiluminescence microscopy for the diagnosis of doubtful melanocytic skin lesions: Comparison of the ABCD rule of dermatoscopy and a new 7-point checklist based on pattern analysis," *Arch. Dermatol.*, vol. 134, no. 12, pp. 1563–1570, 1998.

[2] G. Argenziano, H. P. Soyer, V. D. Giorgio, D. Piccolo, P. Carli, M. Delfino, A. Ferrari, R. Hofmann-Wellenhof, D. Massi, G. Mazzocchetti, M. Scalvenzi, and I. H. Wolf, Dermoscopy, An Interactive Atlas EDRA Medical Publishing, 2000 [Online]. Available: http://www.dermoscopy.org

[3] M. Binder, M. Schwarz, A. Winkler, A. Steiner, A. Kaider, K. Wolff, and M. Pehamberger, "Epiluminescence microscopy. A useful tool for the diagnosis of pigmented skin lesions for formally trained dermatologists," *Arch. Dermatol.*, vol. 131, no. 3, pp. 286–291, 1995.

[4] A. Blake and M. Isard, *Active Contours*. : Springer, 1998.

[5] M. J. Carlotto, "Histogram analysis using a scale-space approach," *IEEE Trans. Pattern Anal. Mach. Intell.*, vol. PAMI-9, no. 1, pp. 121–129, 1987.

[6] M. Celebi, Y. Aslandogan, and P. Bergstresser, "Unsupervised border detection of skin lesion images," in *Int. Conf. Information Technology: Coding and Computing (ITCC 2005)*, 2005, vol. 2, pp. 123–128.

[7] M. Celebi, H. Kingravi, and J. Lee, "Fast and accurate border detection in dermoscopy images using statistical region merging," in *Proc. SPIE Medical Imaging*, 2007.

[8] T. Chan, B. Sandberg, and L. Vese, "Active contours without edges for vector-valued images," *J. Vis. Commun. Image Repres.*, vol. 11, no. 2, pp. 130–141, 2000.

[9] Y. Q. Chen, M. S. Nixon, and D. W. Thomas, "Statistical geometrical features for texture classification," *Pattern Recognit.*, vol. 28, no. 4, pp. 537–552, 1995.

[10] D. H. Chung and G. Sapiro, "Segmenting skin lesions with partial-differential-equations-based image processing algorithms," *IEEE Trans. Med. Imag.*, vol. 19, pp. 763–767, 2000.

[11] B. Erkol, R. H. Moss, R. J. Stanley, W. V. Stoecker, and E. Hva-tum, "Automatic lesion boundary detection in dermoscopy images using gradient vector flow snakes," *Skin Res. & Technol.*, vol. 11, pp. 17–26, 2005.

[12] H. Ganster, P. Pinz, R. Rohrer, E. Wildling, M. Binder, and H. Kittler, "Automated melanoma recognition," *IEEE Trans. Med. Imag.*, vol. 20, pp. 233–239, Mar. 2001.

[13] J. Gao, J. Zhang, and M. G. Fleming, "A novel multiresolution color image segmentation technique and its application to dermatoscopic image segmentation," in *Proc. Int. Conf. Image Processing*, 2000, vol. 3, pp. 408–411.

[14] A. Hammoude, "Computer-Assisted Endocardial Border Identification from a Sequence of Two-Dimensional Echocardiographic Images," Ph.D. dissertation, Univ. Washington, Seattle, WA, 1988.

[15] M. Kass, A. Witkin, and D. Terzopoulos, "Snakes: Active contour models," *Int. J. Comput. Vis.*, vol. 1, no. 14, pp. 321–331, 1987.

[16] Y. W. Lim and S. U. Lee, "On the color image segmentation algorithm based on the thresholding and the fuzzy c-means techniques," *Pattern Recognit.*, vol. 23, no. 9, pp. 935–952, 1990.

[17] J. Maeda, A. Kawano, S. Saga, and Y. Suzuki, "Number-driven perceptual segmentation of natural color images for easy decision of optimal result," in *Proc. Int. Conf. Image Processing*, 2007, vol. 2, pp. 265–268.

[18] J. Maeda, A. Kawano, S. Saga, and Y. Suzuki, "Unsupervised perceptual segmentation of natural color images using fuzzy-based hierarchical algorithm," in *Proc. SCIA*. New York: Springer, 2007, vol. 4522, Lecture Notes in Computer Science, pp. 462–471.

[19] G. McLachlan and T. Krishnan, *The EM Algorithm and Extensions*. New York: Wiley, 1997.

[20] T. Mendonca, A. Marcal, A. Vieira, J. Nascimento, M. Silveira, J. Marques, and J. Rozeira, "Comparison of segmentation methods for automatic diagnosis of dermoscopy images," in *Proc. IEEE Int. Conf. Engineering in Medicine and Biology Society*, 2007, pp. 6572–6575.

[21] F. Nachbar, W. Stolz, T. Merckle, A. B. Cognetta, T. Vogt, M. Landthaler, P. Bilek, O. Braun-Falco, and G. Plewig, "The ABCD rule of dermatoscopy: High prospective value in the diagnosis of doubtful melanocytic skin lesions," *J. Amer. Acad. Dermatol.*, vol. 30, pp. 551–559, 1994.

[22] J. Nascimento and J. S. Marques, "Adaptive snakes using the em algorithm," *IEEE Trans. Image Process.*, vol. 14, pp. 1678–1686, 2005.

[23] S. Osher and J. Sethian, "Fronts propagating with curvature-dependent speed: Algorithms based on Hamilton-Jacobi equations," *J. Comp. Phys*, vol. 79, pp. 12–49, 1988.

[24] N. Otsu, "A threshold selection method from gray-level histograms," *IEEE Trans. Syst., Man, Cybern.*, vol. SMC-9, no. 1, pp. 62–66, 1979.

[25] T. Pavlidis, *Algorithms for Graphics and Image Processing*. Rockville, MD: Computer Science Press, 1982.

[26] P. Rubegni, A. Ferrari, G. Cevenini, D. Piccolo, M. Burroni, R. Perotti, K. Peris, P. Taddeucci, M. Biagioli, G. Dell'Eva, S. Chimenti, and L. Andreassi, "Differentiation between pigmented spitz naevus and melanoma by digital dermoscopy and stepwise logistic discriminant analysis," *Melanoma Res.*, vol. 11, no. 1, pp. 37–44, 2001.
[27] P. Schmid, "Lesion detection in dermatoscopic images using anisotropic diffusion and morphological flooding," in *Proc. Int. Conf. Image Processing*, 1999, vol. 3, pp. 449–453.
[28] P. Schmid, "Segmentation of digitized dermatoscopic images by two-dimensional color clustering," *IEEE Trans. Med. Imag.*, vol. 18, pp. 164–171, 1999.
[29] M. Silveira and J. Marques, "Level set segmentation of dermoscopy images," in *Proc. IEEE Int. Symp. Biomedical Imaging: From Nano to Macro*, 2008.
[30] S. Umbaugh, R. Moss, W. Stoecker, and G. Hance, "Automatic color segmentation algorithms-with application to skin tumor feature identification," *IEEE Eng. Med. Biol. Mag.*, vol. 12, no. 3, pp. 75–82, Sep. 1993.
[31] S. E. Umbaugh, R. H. Moss, W. V. Stoecker, and G. A. Hance, "Automatic color segmentation algorithms-with application to skin tumor feature identification," *IEEE Eng. Med. Biol. Mag.*, vol. 12, no. 3, pp. 75–82, 1993.
[32] C. Xu and J. Prince, "Snakes, shapes, and gradient vector flow," *IEEE Trans. Image Process.*, vol. 7, no. 3, pp. 359–369, Mar. 1998.

Margarida Silveira (M'02) received the E.E. and Ph.D. degrees from the Technical University of Lisbon, Lisbon, Portugal, in 1994 and 2004, respectively.

Currently, she is an Assistant Professor with the Electrical Engineering Department, Instituto Superior Técnico, Lisbon, and a Researcher at the Institute for Systems and Robotics. Her research interests are in the areas of image processing, computer vision, and pattern recognition.

Jacinto C. Nascimento (M'06) received the E.E. degree from the Instituto Superior de Engenharia de Lisboa, Lisbon, Portugal, in 1995 and the M.Sc. and Ph.D. degree from Instituto Superior Técnico, Lisbon, in 1998 and 2003, respectively.

Presently, he is a Posdoctorate Researcher at the Instituto Superior Técnico, Lisbon, affiliated with the Institute for Systems and Robotics (ISR). His research interests are image processing, shape tracking, robust estimation, medical imaging, and video surveillance.

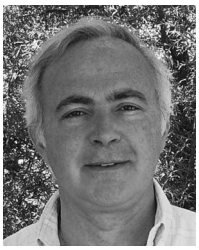

Jorge S. Marques received the E.E. and Ph.D. degrees, and the aggregation title, from the Technical University of Lisbon, Lisbon, Portugal, in 1981, 1990, and 2002, respectively.

Currently, he is an Associate Professor with the Electrical Engineering Department, Instituto Superior Técnico, Lisbon, and a Researcher at the Institute for Systems and Robotics. He has published over 150 papers in international journals and conferences and is the author of the book *Pattern Recognition: Statistical and Neural Methods* (in Portuguese) (Lisbon, Portugal: IST, 2005, 2nd ed.). His research interests are in the areas of statistical image processing, shape analysis, and pattern recognition.

André R. S. Marçal (M'02) received the degree in physics (solid-state physics) from the University of Porto, Porto, Portugal, in 1991, and the M.Sc. and Ph.D. degrees in remote sensing and image processing from the University of Dundee, Dundee, Scotland, in 1994 and 1998, respectively.

He has been an Assistant Professor at the Applied Mathematics Department, University of Porto, since 1999, and the Secretary General of the European Association of Remote Sensing Laboratories (EARSeL) since 2005.

Dr. Marçal received the prize for the best Ph.D. from the Remote Sensing Society (U.K.) in 1999.

Teresa Mendonça (M'03) was born in Porto, Portugal. She received the applied mathematics degree in 1981 and the Ph.D. degree in applied mathematics (systems theory and signal processing) in 1993, both from the Faculdade de Ciências da Universidade do Porto (FCUP).

She is currently an Assistant Professor in the Department of Applied Mathematics at FCUP and Researcher in the Mathematical Systems Theory Group, UI&D Matematica e Aplicações, Universidade de Aveiro, Portugal. Her research interests are in the area of mathematical systems theory and control, system identification and control in biomedical applications, and image processing.

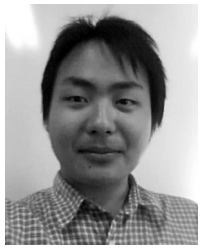

Syogo Yamauchi received the B.E. degree in computer science and systems engineering in 2007 from Muroran Institute of Technology, Muroran, Japan. where he is currently pursuing the M.E. degree in the Division of Computer Science and Systems Engineering.

His research interests include image segmentation and computer vision.

Junji Maeda (M'94) received the B.S. degree in physics and the M.E. and Ph.D. degrees in applied physics from Hokkaido University, Hokkaido, Japan.

From 1974 to 1987, he was an Assistant Professor in the Department of Applied Physics, Hokkaido University. In 1988, he joined Muroran Institute of Technology, Muroran, Japan, where he is currently a Professor in the Department of Computer Science and Systems Engineering. His research interests include image processing, computer vision, and pattern recognition.

Jorge Rozeira is the Director of the Dermatology Service of the Hospital Pedro Hispano, Matosinhos, Portugal. He is a pioneer of telemedicine and teledermatology in Portugal.